Methanol synthesis from CO2 hydrogenation over a Pd4/In2O3 model catalyst: A combined DFT and kinetic study

ARTICLE *in* JOURNAL OF CATALYSIS · AUGUST 2014

Impact Factor: 6.92 · DOI: 10.1016/j.jcat.2014.06.002

4 AUTHORS:

Jingyun Ye
University of Pittsburgh
14 PUBLICATIONS **209** CITATIONS
SEE PROFILE

Chang-Jun Liu
Tianjin University
153 PUBLICATIONS **3,402** CITATIONS
SEE PROFILE

Donghai Mei
Pacific Northwest National Laboratory
102 PUBLICATIONS **2,157** CITATIONS
SEE PROFILE

Qingfeng Ge
Southern Illinois University Carbondale
129 PUBLICATIONS **2,730** CITATIONS
SEE PROFILE

Journal of Catalysis 317 (2014) 44–53

Contents lists available at ScienceDirect

Journal of Catalysis

journal homepage: www.elsevier.com/locate/jcat

Methanol synthesis from CO_2 hydrogenation over a Pd_4/In_2O_3 model catalyst: A combined DFT and kinetic study

Jingyun Ye [a,b], Chang-jun Liu [a], Donghai Mei [c], Qingfeng Ge [a,b,*]

[a] School of Chemical Engineering and Technology, Tianjin University, Tianjin 300072, China
[b] Department of Chemistry and Biochemistry, Southern Illinois University, Carbondale, IL 62901, USA
[c] Institute for Integrated Catalysis, Pacific Northwest National Laboratory, Richland, WA 99352, USA

ARTICLE INFO

Article history:
Received 20 September 2013
Revised 26 May 2014
Accepted 3 June 2014

Keywords:
Methanol synthesis
Carbon dioxide
Indium oxide
Palladium
Density functional theory
Kinetic modeling

ABSTRACT

Methanol synthesis from CO_2 hydrogenation on a model Pd/In_2O_3 catalyst, i.e. Pd_4/In_2O_3, has been investigated using density functional theory (DFT) and microkinetic modeling. Three possible routes in the reaction network of $CO_2 + H_2 \rightarrow CH_3OH + H_2O$ have been examined. Our DFT results show that the HCOO route competes with the RWGS route whereas a high activation barrier blocked the HCOOH route kinetically. The DFT results also suggest that $H_2COO^* + H^* \leftrightarrow H_2CO^* + OH^*$ and cis-$COOH^* + H^* \leftrightarrow CO^* + H_2O^*$ are the rate-limiting steps in the HCOO route and the RWGS route, respectively. Microkinetic modeling results demonstrate that the HCOO route is the dominant pathway for forming methanol from CO_2 hydrogenation. Furthermore, the activation of the H adatom on the Pd cluster and the presence of H_2O on the In_2O_3 substrate play important roles in promoting methanol production. The hydroxyl adsorbed at the interface of Pd_4/In_2O_3 induces structural transformation of the supported Pd_4 cluster from a butterfly shape into a tetrahedron one. This structural change not only indicates the dynamical nature of the supported nanocatalysts during the reaction but also causes the final hydrogenation step to change from CH_3O to H_2COH.

1. Introduction

Hydrogenation of CO_2 into methanol has attracted attention worldwide for its role in chemical sequestration of CO_2 [1–4]. Many catalysts have been exploited for this reaction and among them, supported Pd catalysts including Pd/Ga_2O_3 [5], Pd/CeO_2 [6], Pd/ZnO [7] and Pd/ZrO_2 [8] have shown high activity. For supported Pd catalysts, the supports and promoters (mostly metal oxides) play important roles in the activity and selectivity for methanol production. For example, the effect of metal oxide supports has been found to follow the order of $Ga_2O_3 > ZnO > Al_2O_3 > TiO_2 \approx Cr_2O_3 > SiO_2 \approx ZrO_2$ [5]. Bonivardi et al. showed that the addition of Ga_2O_3 into a Pd/SiO_2 catalyst increases the turnover rate by 500-fold and the selectivity toward methanol to 70% from 17% as compared with those on the clean Pd/SiO_2 [9]. Iwasa and coworkers suggested that the remarkable activity and selectivity of Pd/Ga_2O_3 catalysts for either methanol synthesis or for the methanol stream reforming were a consequence of Pd–Ga alloy formation [10,11]. The roles of metal oxides are summarized as: (1) the metal oxides help to disperse and stabilize the Pd particles or form bi-metallic particles due to their strong interactions with Pd; (2) the metal oxides (basic or amphoteric) generally have a higher affinity toward CO_2, and are thereby beneficial for CO_2 adsorption and activation; (3) the carbon monoxide ascribed to the reverse water–gas shift (RWGS) mainly proceeds on the metal oxides since Pd has a low activity for the RWGS reaction [5].

In_2O_3 has been well known for its unique physical properties of optical transparency and electrical conductivity [12–16]. However, the interesting catalytic properties of In_2O_3 have not attracted much attention until recently [17–22]. The Pd/In_2O_3 catalyst showed high selectivity for CO_2, and correspondingly low CO productivity, in the methanol steam reforming (MSR) for hydrogen production and this was attributed to formation of the Pd–In alloy at low temperatures [10,22–27]. Iwasa et al. reported that methanol can be produced from CO_2 as a feed gas with H_2 on Pd/In_2O_3, but not from CO [28]. Since methanol steam reforming is the reversal of methanol synthesis from CO_2 hydrogenation, methanol formation from CO_2 hydrogenation on Pd/In_2O_3 is expected to go through the direct hydrogenation of CO_2.

The interfacial sites are unique to the supported metal catalyst and play an important role in heterogeneous catalysis. The synergetic effect of H_2 dissociation on Pd particles and the spillover of

* Corresponding author at: Department of Chemistry and Biochemistry, Southern Illinois University, Carbondale, IL 62901, USA.
E-mail address: qge@chem.siu.edu (Q. Ge).

http://dx.doi.org/10.1016/j.jcat.2014.06.002
0021-9517/

the H adatoms to the support where CO_2 is adsorbed play important roles for methanol synthesis from CO_2 hydrogenation [29–31]. Very recently, Kwak et al. demonstrated that atomically dispersed Pd assisted by oxides, either as support (Al_2O_3) or promoter (La_2O_3), exhibits activity toward CO_2 reduction whereas Pd supported on a carbon nanotube support without oxide does not [32]. In fact, atomically dispersed supported metal catalysts have become an intensely focused area of research in recent years [33–37]. H_2 adsorption and dissociation on the pure Pd surfaces or particles have been studied both experimentally [31,38] and theoretically [39–41]. The interaction of H_2 and Pd is closely related to the H_2 pressure and particle size of Pd. The strong interaction between H atoms and the small Pd particles (Pd_n, $n = 3, 4$) results in incorporation of the H atoms into the Pd cluster [40], which strongly suppresses the activity of H for CO_2 hydrogenation. Consequently, activation of the strongly bound H atoms needs to be taken into account in CO_2 hydrogenation, especially on a supported Pd nanoparticle. In addition, the dissociation of H_2, H_2O and other intermediates (i.e. COOH, HCOOH, H_2COOH) produces a large amount of hydroxyls during the reaction, which are likely to adsorb on the In_2O_3 surface [18,20,21]. As a result, the effect of hydroxyls on the reaction mechanism has also to be examined carefully. For example, studies of CO_2 hydrogenation on Ni_4/γ-Al_2O_3 [42] indicate that the hydroxyls on the γ-Al_2O_3 support alter the reaction pathway for CO_2 hydrogenation and ultimately affect the distribution of the final products.

Previously, theoretical studies of methanol synthesis from CO_2 were carried out on a pure metal surface (Cu(1 1 1) [43–45]), a metal cluster (Cu_{29} [44]), a metal doped Cu surface [46] or a bare metal oxide (ZnO [47]). On the supported metal catalysts, the adsorption and dissociation of H_2 usually occur on the surface of the metal particle. Murray et al. found that carbon monoxide oxidation in ceria-based catalysts is greatly enhanced at the ceria–metal interface sites for a range of group VIII metal catalysts [48]. Heiz et al. reported that a single Pd atom supported on MgO is active for the production of benzene, but a free Pd atom is inert for this reaction [49]. The activity of Pd/MgO was attributed to the charge transfer from the support to the metal cluster as revealed by the DFT study. In fact, models such as Pd_n/MgO [49] and Ni_4/γ-Al_2O_3 [42] become attractive model systems. These simplified model systems capture key features of the metal–support interaction and provide interfacial sites as active sites for the catalytic transformation whereas quantitative agreement with the experimental system is generally not anticipated. Since CO_2 generally physisorbs on metallic Pd [50–52], the hydrogenation of CO_2 likely utilizes hydrogen adatoms generated on Pd and proceeds at the interface of the metal particle and the support. Herein, a Pd_4 cluster supported on In_2O_3 (Pd_4/In_2O_3) was designed as a model catalyst to elucidate the mechanism of methanol synthesis from CO_2 hydrogenation using a combination of density functional theory calculation and microkinetic study. The effects of H adatom activation, water and hydroxyl on the reaction mechanism and kinetics were also examined. The results confirmed that Pd on In_2O_3 would be a good catalyst for methanol synthesis from CO_2 hydrogenation.

2. Methodology and models

All the calculations were performed using the Vienna ab initio simulation package (VASP) [53–55], a periodic DFT code with projector augmented wave (PAW) potentials. The nonlocal exchange correlation energy was evaluated using the Perdew–Burke–Ernzerhof functional [56]. The 5s and 5p states of In were treated explicitly as valence states within the scalar-relativistic PAW approach [57]. A plane wave basis set with a cutoff energy of 400 eV and a $(2 \times 2 \times 1)$ k-point grid generated with the Monkhorst–Pack scheme were found to give converged results. The atomic structures were relaxed using either the conjugate gradient algorithm or the quasi-Newton scheme as implemented in the VASP code until the forces on all unconstrained atoms were less than 0.03 eV/Å.

The $In_2O_3(1\,1\,0)$ surface is modeled with a $(1 \times \sqrt{2})$ supercell, built from the optimized In_2O_3 bulk unit cell with lattice parameters $a = b = c = 10.18$ Å [19,20]. The supercell has a dimension of 10.18 Å × 14.40 Å × 17.96 Å. The surface slab consists of 48 O atoms and 32 In atoms distributed in four atomic layers and is separated by a vacuum of 12 Å. The optimized Pd_4 cluster with a tetrahedral structure is supported on the $In_2O_3(1\,1\,0)$ surface to generate the Pd_4/In_2O_3 model catalyst. In all calculations, atoms in the bottom two layers of the $In_2O_3(1\,1\,0)$ slab are frozen at their equilibrium bulk positions whereas those in the top two layers together with the Pd_4 cluster and other species involved in methanol synthesis are allowed to relax. Test calculations by increasing the vacuum space to 15 Å showed that the adsorption energy of CH_3OH is −0.78 eV, almost exactly the same as that from the slab with 12 Å vacuum. The reaction energy and activation barrier for bi-$HCOO^* + H^* \rightarrow H_2COO^* + *$, an elementary step in methanol formation, are +0.77 eV and 1.10 eV, respectively, also very close to those (+0.75 eV and 1.09 eV, respectively) from the slab with 12 Å vacuum.

The adsorption energies of intermediates were defined as:

$$\Delta E_{ad}(M) = E_{M/(Pd_4/In_2O_3)} - E_{(Pd_4/In_2O_3)} - E_{(M)}$$

where M represents molecules, intermediates involved in methanol synthesis as well as their corresponding products upon adsorption. $E_{M/(Pd_4/In_2O_3)}$, $E_{(Pd_4/In_2O_3)}$ and $E_{(M)}$ represent the total energies of the Pd_4/In_2O_3 with the adsorbate and the clean Pd_4/In_2O_3, the free molecule or intermediate, respectively. In the case of co-adsorption and reaction on the surface, the relative energies were computed with respect to the sum of the total energies of the corresponding free molecules. According to the above definition, negative values indicate that the process is exothermic whereas positive values indicate that the process is endothermic. Transition states along a reaction pathway were determined in two steps: First, the nudged elastic band method [58], typically with 7–9 images was used to locate the likely transition state; second, the likely transition state was relaxed using the quasi-Newton algorithm with the same force convergence criterion. The relaxed transition state was then confirmed through frequency analysis.

3. Results and discussion

3.1. Pd_4 supported on $In_2O_3(1\,1\,0)$

The side and top views of $In_2O_3(1\,1\,0)$ and $Pd_4/In_2O_3(1\,1\,0)$ are shown in Fig. 1. The structure of $In_2O_3(1\,1\,0)$ has been discussed in our previous papers in detail [19,20]. In the present study, we focus on $Pd_4/In_2O_3(1\,1\,0)$. The optimized Pd_4 cluster is a tetrahedron in the gas phase [59]. The initial $Pd_4/In_2O_3(1\,1\,0)$ structure was built by placing the optimized Pd_4 cluster on the $In_2O_3(1\,1\,0)$ surface. After relaxation, the Pd_4 cluster is stabilized on the surface by bridging between the two In–O chains through the Pd–In and the Pd–O bonds (Pd_1–In_2: 2.62 Å, Pd_3–In_4': 2.78 Å, Pd_4–O_2: 2.16 Å, Pd_4–O_4': 2.13 Å, Pd_2–O_3: 2.11 Å, Pd_2–O_5': 2.11 Å). We note that the original tetrahedral structure of Pd_4 was distorted into a butterfly shape after optimization. The average Pd–Pd bond length is shortened from 2.61 Å in a Pd_4 tetrahedron to 2.56 Å. The angles of $\angle Pd_{1\text{-}4\text{-}3}$ and $\angle Pd_{1\text{-}2\text{-}3}$ are opened from 60° to ~85.0°, whereas the dihedral angle between the $Pd_{1\text{-}2\text{-}4}$ plane and the $Pd_{3\text{-}2\text{-}4}$ plane is opened from 70.5° to 105.6°. The $Pd_4/In_2O_3(1\,1\,0)$ structure is

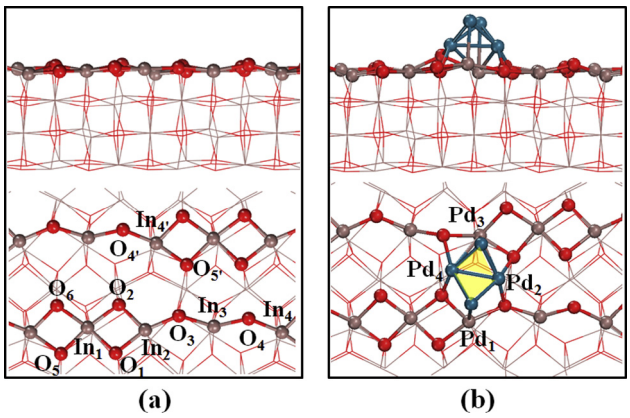

Fig. 1. Optimized structure of (a) In_2O_3 (1 1 0) surface; (b) Pd_4 supported on In_2O_3 (1 1 0). Red: O atoms; Brown: In atoms; blue: Pd atoms. (For interpretation of the references to color in this figure legend, the reader is referred to the web version of this article.)

similar to Pd_4/γ-Al_2O_3(1 0 0) and Pd_4/γ-Al_2O_3(1 1 0) reported by Valero et al. [60,61]. The adsorption energy of Pd_4 on In_2O_3 is −4.37 eV. This result indicates that the Pd_4 cluster binds the In_2O_3(1 1 0) surface much stronger than it does the γ-Al_2O_3(1 1 0) surface and an exothermic process is expected when loading Pd_4 on the In_2O_3 surface. We also note that Pd_4 is a rather small cluster and has a cohesive energy of 1.68 eV/atom. Loading the Pd_4 cluster on In_2O_3(1 1 0) increases the cohesive energy by 1.02 eV/atom to 2.70 eV/atom. However, this value is still significantly smaller than either the bulk cohesive energies of Pd (3.99 eV/atom calculated and 3.89 eV/atom experimental [62,63]) or the averaged bulk cohesive energy of PdIn (3.57 eV/atom). The calculated cohesive energies are summarized in Table S1 for comparison. Based on the calculated cohesive energies, the following order of stability can be obtained: Pd bulk > PdIn bulk > Pd_4/In_2O_3 > Pd_4. The results indicated that the highly dispersed Pd particles, in particular the particles as small as Pd_4, tend to agglomerate. It may also form bulk PdIn alloy under the highly reducing conditions. In fact, deactivation due to sintering is a common and critical issue that needs to be addressed in the development of new catalysts [64–67]. The development of nanomanufacturing in the past decade is expected to provide a solution to issues such as sintering [33,68,69]. The stabilization of Pd_4 due to In_2O_3 makes it a potentially useful model catalyst. In addition, Pd_4 provides both metal–support and pure metal–metal interaction in the 3D arrangement. The interfacial sites will be available for CO_2 adsorption and allow H adatoms produced on the Pd particle to react with the adsorbed CO_2.

3.2. CO_2 and H_2 adsorption and dissociation

We first studied the CO_2 adsorption on the Pd_4/In_2O_3(1 1 0) surface. Three typical configurations (CO_2_1, CO_2_2, CO_2_3) of CO_2 adsorption on Pd_4/In_2O_3 are shown in Fig. 2. CO_2_1, CO_2_2, CO_2_3, representing CO_2 adsorption at three types of sites: the interface of Pd cluster and In_2O_3 substrate, the top of Pd cluster and the surface of In_2O_3, respectively. The calculated CO_2 adsorption energies in the three configurations are −0.37 eV, −0.41 eV and +0.03 eV, respectively.

H_2 dissociative adsorption is an important step in CO_2 hydrogenation. On Pd_4/In_2O_3, H_2 dissociates spontaneously and forms two H adatoms on the supported Pd_4 cluster, shown in Fig. 2 (H_2_dis). The dissociative adsorption energy of hydrogen is −1.08 eV. According to our previous definition [20], H_2 dissociates on the Pd cluster into two hydridic H adatoms (Pd–H). Once the spillover of H adatoms from the Pd cluster to the In_2O_3 surface took place, those H adatoms binding the surface O atoms are oxidized to proton-like in the form of hydroxyl (O–H), whereas others binding the surface In atoms (In–H) remain hydridic. The proton-like H adatoms can hydroxylate the adsorbed CO_2 through proton transfer to the O atom of CO_2, whereas hydridic H adatoms will hydrogenate CO_2 by attacking the C atom of the adsorbed CO_2.

The CO_2 dissociation is studied at the interface of Pd/In_2O_3 since CO produced from the dissociation would be the reactant for methanol synthesis. As shown in Fig. 3, R25 and R25′ are two reactions for CO_2 dissociation, resulting in different CO adsorption configurations, CO_b^* and CO_i^*. R25 is endothermic by +0.79 eV with an activation barrier of 1.41 eV, whereas R25′ is endothermic by +1.40 eV with an activation barrier of 2.71 eV. Due to the high barriers for CO_2 dissociation, direct dissociation of CO_2 is not expected to contribute to methanol formation. CO_2 dissociation had also been studied on other metal oxides. For example, the reported activation barriers are 0.38 eV on Cu/ZrO_2 [70] and 0.39 eV on ZnO [47]. However, the O adatoms produced from CO_2 dissociation on those surfaces are difficult to remove, thereby blocking the active sites for further reaction [70]. The results indicate that the possibility of a Pd/In_2O_3 catalyst is capable of avoiding deactivation originated from the O adatoms due to CO_2 dissociation.

The adsorbed CO_2 in both CO_2_1 and CO_2_2 is stable for subsequent CO_2 hydrogenation while the adsorbed CO_2 in CO_2_3 prefers to desorb or be transformed to CO_2_1, indicating that the CO_2 molecule prefers to adsorb at the interface or on the supported Pd cluster. On the other hand, the high dissociative adsorption energy of H_2 on the supported Pd_4 cluster not only indicates the strong capability of the Pd_4 cluster for H_2 dissociation but also suggests a possibility of high H coverage on the Pd cluster. Consequently, the dissociative adsorption of H_2 prevails on the Pd cluster, pushing CO_2 to adsorb at the interfacial sites. As such,

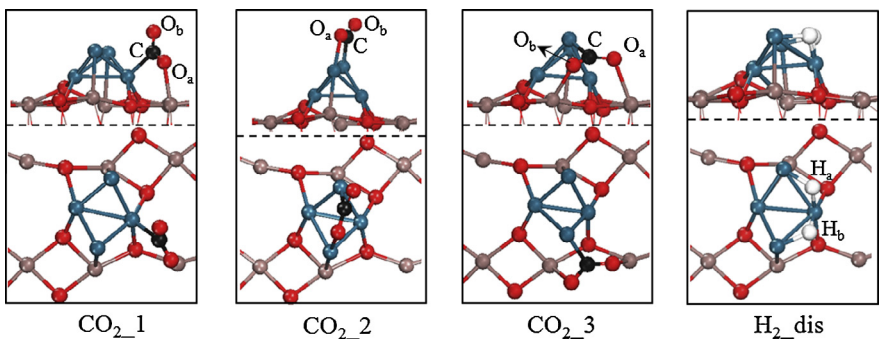

Fig. 2. Optimized structures of adsorbed CO_2 and dissociated H_2 on Pd_4/In_2O_3. Black: C atom; White: H atom.

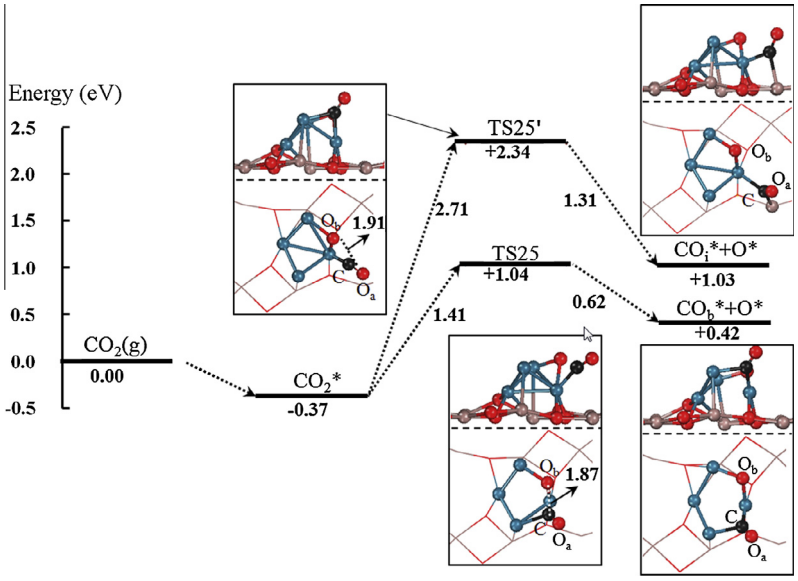

Fig. 3. Potential energy profile of two pathways for CO_2 dissociation to form CO.

CO_2 hydrogenation is more likely to occur at the Pd_4/In_2O_3 interface (CO_2_1).

3.3. Methanol synthesis at the interface of Pd_4/In_2O_3

The reaction network of methanol synthesis from CO_2 hydrogenation shown in Fig. 4 includes the formate (HCOO), reverse water–gas shift (RWGS) and formic acid (HCOOH) routes. All the structural parameters and adsorption energies of the reaction intermediates involved in these reaction pathways are summarized in Table 1. The corresponding optimized structures are given in the supporting information (Fig. S1). All the reaction energies and barriers of the elementary steps are summarized in Table 2. The structural details of initial reactants, transition states and finial products are shown in the support information (Fig. S2). The adsorption of CO_2 at the interface of Pd_4/In_2O_3 is exothermic by −0.37 eV with a bent structure, which indicates the interfacial site facilitates not only the CO_2 capturing but also the CO_2 activation. In such a way, the Pd_4 cluster provides a flow of atomic H for CO_2 hydrogenation. The interface of Pd_4/In_2O_3 provides the active site for CO_2 hydrogenation. As a result, the three reaction routes share the same starting point, CO_2_1.

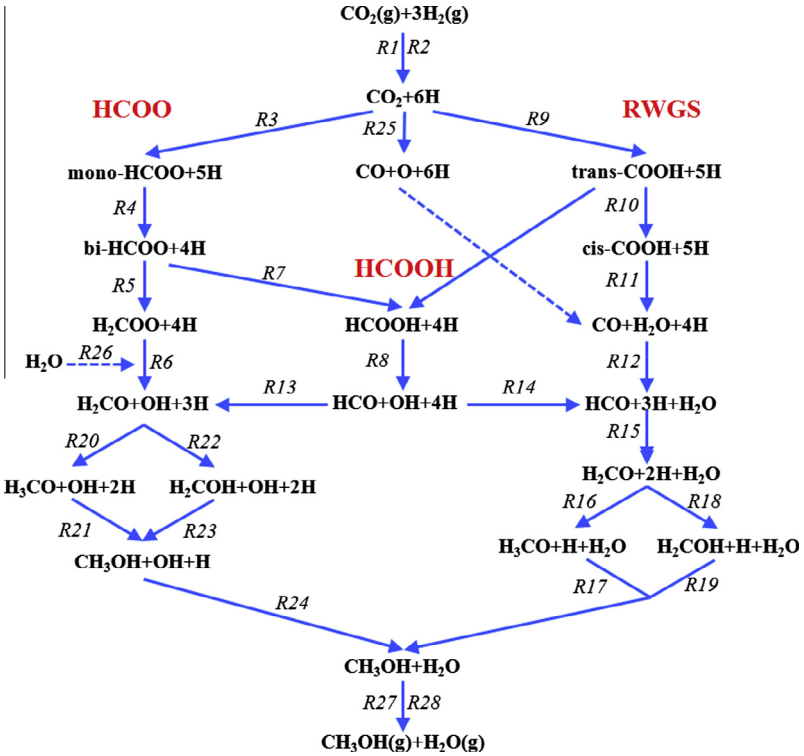

Fig. 4. Reaction network of methanol synthesis from CO_2 and H_2 on Pd_4/In_2O_3.

Table 1
Adsorption energies E_{ad} (eV) and geometric parameters of all reaction intermediates in methanol synthesis on Pd_4/In_2O_3.

Species	E_{ad} (eV)	Bond type and bond length (Å)
H	−3.04	$d_{(Pd2-H)}$ = 1.74, $d_{(Pd3-H)}$ = 1.70
O	−3.94	$d_{(Pd1-O)}$ = 2.02, $d_{(Pd3-O)}$ = 1.91
OH	−3.45	$d_{(Pd1-O)}$ = 2.09, $d_{(In2-O)}$ = 2.19, $d_{(O-H)}$ = 0.98
H_2O	−0.58	$d_{(In1-O)}$ = 2.39, $d_{(O-Ha)}$ = 0.98, $d_{(O-Hb)}$ = 0.98
CO_b	−1.65	$d_{(Pd1-C)}$ = 2.02, $d_{(Pd2-C)}$ = 1.91, $d_{(C-Oa)}$ = 1.19
CO_i	−0.88	$d_{(Pd3-C)}$ = 2.05, $d_{(In3-C)}$ = 2.44, $d_{(C-Oa)}$ = 1.18
CO_2	−0.37	$d_{(Pd2-C)}$ = 2.09, $d_{(In3-Oa)}$ = 2.26, $d_{(C-Oa)}$ = 1.22, $d_{(C-Ob)}$ = 1.26
HCO	−2.55	$d_{(Pd1-C)}$ = 2.13, $d_{(Pd2-C)}$ = 2.01, $d_{(In3-Oa)}$ = 2.37, $d_{(C-Oa)}$ = 1.26, $d_{(C-H1)}$ = 1.12
mono-HCOO	−2.29	$d_{(In3-Oa)}$ = 2.18, $d_{(C-Oa)}$ = 1.29, $d_{(C-Ob)}$ = 1.22, $d_{(C-H1)}$ = 1.18
bi-HCOO	−2.98	$d_{(In3-Oa)}$ = 2.26, $d_{(In2-Ob)}$ = 2.34, $d_{(C-Oa)}$ = 1.26, $d_{(C-Ob)}$ = 1.29, $d_{(C-H1)}$ = 1.11
trans-COOH	−2.51	$d_{(In3-Oa)}$ = 2.38, $d_{(C-Oa)}$ = 1.26, $d_{(C-Ob)}$ = 1.37, $d_{(C-H1)}$ = 0.99
cis-COOH	−2.58	$d_{(In3-Oa)}$ = 2.35, $d_{(C-Oa)}$ = 1.27, $d_{(C-Ob)}$ = 1.37, $d_{(C-H1)}$ = 0.99
H_2COO	−4.14	$d_{(In3-Oa)}$ = 2.14, $d_{(In2-Ob)}$ = 2.19, $d_{(C-Oa)}$ = 1.35, $d_{(C-Ob)}$ = 1.49, $d_{(C-H1)}$ = $d_{(C-H2)}$ = 1.11
HCOOH	−0.52	$d_{(In3-Oa)}$ = 2.34, $d_{(C-Oa)}$ = 1.23, $d_{(C-Ob)}$ = 1.35, $d_{(C-H1)}$ = 1.10, $d_{(O-H2)}$ = 0.99
H_2CO	−0.90	$d_{(In3-Oa)}$ = 2.25, $d_{(C-Oa)}$ = 1.29, $d_{(C-H1)}$ = $d_{(C-H2)}$ = 1.11
H_3CO	−1.90	$d_{(In3-Oa)}$ = 2.15, $d_{(C-Oa)}$ = 1.35, $d_{(C-H1)}$ = $d_{(C-H2)}$ = 1.11, $d_{(C-H3)}$ = 1.21
H_2COH	−1.85	$d_{(In3-Oa)}$ = 2.45, $d_{(C-Oa)}$ = 1.44, $d_{(C-H1)}$ = $d_{(C-H2)}$ = 1.10, $d_{(O-H3)}$ = 0.98
CH_3OH	−0.78	$d_{(In3-Oa)}$ = 2.32, $d_{(C-Oa)}$ = 1.44, $d_{(C-H1)}$ = $d_{(C-H2)}$ = $d_{(C-H3)}$ = 1.10, $d_{(O-H4)}$ = 1.01

Table 2
Reaction energies ΔE (eV) and activation barriers E_a (eV) of each elementary step involved in methanol synthesis on Pd_4/In_2O_3.

No.	Reaction	ΔE (eV)	E_a (eV)
R1	$CO_2(g) + {}^* \rightarrow CO_2^*$	−0.37	–
R2	$H_2(g) + {}^* + {}^* \rightarrow 2H^*$	−1.08	0
R3	$CO_2^* + H^* \rightarrow$ mono-$HCOO^* + {}^*$	+0.81	1.17
R4	mono-$HCOO^* \rightarrow$ bi-$HCOO^*$	−0.68	–
R5	bi-$HCOO^* + H^* \rightarrow H_2COO^* + {}^*$	+0.75	1.09
R6	$H_2COO^* + H_s^* \rightarrow H_2CO^* + OH^*$	−1.15	0.89
R7	bi-$HCOO^* + H^* \rightarrow HCOOH^* + {}^*$	+0.12	0.94
R8	$HCOOH^* + {}^* \rightarrow HCO^* + OH^*$	−0.05	2.68
R9	$CO_2^* + H^* \rightarrow$ trans-$COOH^* + {}^*$	+0.21	1.01
R10	trans-$COOH^* \rightarrow$ cis-$COOH^*$	+0.01	0.39
R11	cis-$COOH^* + H^* \rightarrow CO^* + H_2O^*$	+0.26	1.90
R12	$CO_b^* + H^* \rightarrow HCO^* + {}^*$	+0.89	1.36
R12′	$CO_i^* + H^* \rightarrow HCO^* + {}^*$	−0.10	1.19
R13	$HCO^* + H^* + OH^* \rightarrow H_2CO^* + OH^* + {}^*$	+0.67	1.94
R14	$HCO^* + OH^* + H^* \rightarrow HCO^* + H_2O^* + {}^*$	−0.19	1.44
R15	$HCO^* + H^* \rightarrow H_2CO^* + {}^*$	+0.21	0.82
R16	$H_2CO^* + H^* \rightarrow H_3CO^* + {}^*$	+0.03	0.41
R17	$H_3CO^* + H^* \rightarrow CH_3OH^* + {}^*$	+0.24	1.33
R18	$H_2CO^* + H^* \rightarrow H_2COH^* + {}^*$	+1.17	2.20
R19	$H_2COH^* + H^* \rightarrow CH_3OH^* + {}^*$	−1.22	0.26
R20	$H_2CO^* + H^* + OH^* \rightarrow H_3CO^* + OH^* + {}^*$	−0.18	1.09
R21	$H_3CO^* + H^* + OH^* \rightarrow CH_3OH^* + OH^* + {}^*$	+0.25	0.31
R22	$H_2CO^* + H^* + OH^* \rightarrow H_2COH^* + OH^* + {}^*$	+0.76	0.84
R23	$H_2COH^* + H^* + OH^* \rightarrow CH_3OH^* + OH^* + {}^*$	+0.20	1.11
R24	$CH_3OH^* + OH^* + H^* \rightarrow CH_3OH^* + H_2O^* + {}^*$	−0.65	0.98
R25	$CO_2^* + {}^* \rightarrow CO_b^* + O^*$	+0.79	1.41
R25′	$CO_2^* + {}^* \rightarrow CO_i^* + O^*$	+1.40	2.71
R26	$H_2COO^* + H_2O^* \rightarrow H_2CO + 2OH^*$	+0.64	0.72
R27	$CH_3OH^* \rightarrow CH_3OH(g) + {}^*$	+0.78	–
R28	$H_2O^* \rightarrow H_2O(g) + {}^*$	+0.58	–

3.3.1. Formate route

Fig. 5 shows the potential energy surface of the formate route for methanol synthesis from CO_2 hydrogenation. Both pathways share the steps from CO_2 to H_2CO, but branch into different routes before reaching methanol.

The formate route initiates by the direct hydrogenation of adsorbed CO_2 to yield mono-HCOO. This reaction is endothermic by +0.81 eV with an activation barrier of 1.17 eV. The transition state is TS3. The mono-HCOO species is not stable and quickly transforms to a stable bi-HCOO configuration. The transformation is exothermic by −0.68 eV without a barrier [44,47,70–73]. The bi-HCOO further reacts with adsorbed H (H^*) on the Pd cluster and produces H_2COO. This reaction is endothermic by +0.75 eV with an activation barrier of 1.09 eV. The transition state of this step is TS5. Hydrogenation of H_2COO is the next step. Since the H adatom is close to the O atom of the H_2COO species, the $H_2COO^* + H^* \rightarrow H_2COOH^* + {}^*$ step is most likely to happen at the interface. Interestingly, once the H adatom binds to the O atom, the C–O bond of H_2COO breaks simultaneously. This reaction is therefore labeled as $H_2COO^* + H_s^* \rightarrow H_2CO^* + OH^*$ in which H_s^* represents the H adatom on the Pd_4 cluster through a single Pd–H bond. This step is exothermic by −1.15 eV with an activation barrier of 0.89 eV. In fact, the H adatom prefers to bind on the Pd_4 cluster through a Pd–H–Pd (H_b^*) bridging bond, which is 0.91 eV lower than H_s^*. This reveals that activation of H_b^* to H_s^* from the most favorable adsorption configuration is a necessary step for H_2COO hydrogenation. As a result, the reaction barrier increases to 1.80 eV by including the energy of H_b^* activation. The effects of the H adatom activation will be further discussed in the context of hydrogen coverage effect in Section 3.4. Subsequent hydrogenation of H_2CO could go through either H_3CO or H_2COH intermediates via the reactions of R20 ($H_2CO^* + H_{in}^* + OH^* \rightarrow H_3CO^* + OH^* + {}^*$, ΔE = −0.18 eV, E_a = 1.09 eV) or R22 ($H_2CO^* + H_O^* + OH^* \rightarrow H_2COH^* + OH^* + {}^*$, ΔE = +0.76 eV, E_a = 0.84 eV), respectively. The above elementary steps show that hydrogenation of H_2CO to produce CH_3O is thermodynamically more favorable than to produce CH_2OH but kinetically less favorable. CH_3OH can then be produced via H_3CO protonation (R21: $H_3CO^* + H^* + OH^* \rightarrow CH_3OH^* + OH^*$, ΔE = +0.25 eV, E_a = 0.31 eV) or H_2COH hydrogenation (R23: $H_2COH^* + H^* + OH^* \rightarrow CH_3OH^* + OH^*$, ΔE = +0.20 eV, E_a = 1.11 eV). Both reactions are endothermic, but the barrier for the protonation of H_3CO is much lower than that for the hydrogenation of H_2COH. The final step is H_2O production from the $OH^* + H^* \rightarrow H_2O^* + {}^*$ reaction. The last step is an exothermic reaction (ΔE = −0.65 eV) with an activation barrier of 0.98 eV. CH_3OH and H_2O proceed to desorb from the catalyst surface with an overall energy cost of 1.36 eV. Comparing those two reaction pathways, the H_2COH pathway is energetically more favorable than the CH_3O pathway. In presence of OH, the tetrahedral structure of Pd_4 cluster is maintained throughout the steps leading to CH_3OH. Thus, the rate-limiting step is the hydrogenation of H_2COO to H_2CO and OH (R6) based on the energetic analysis.

Previously, we studied CO_2 adsorption and hydrogenation on In_2O_3 and demonstrated that CO_2 could be hydrogenated by the H adatom on the In sites [20]. Furthermore, when the oxygen vacancies were created on the In_2O_3 surface, methanol formation from CO_2 hydrogenation becomes facile [19]. In the present study, we focus on the interfacial sites and examine their role in methanol synthesis. On the basis of calculated potential energy profile, the oxygen vacancy sites are more active for hydrogenation to methanol. On the other hand, H adatoms are generated on the Pd sites, making the interfacial sites spatially advantages for CO_2 hydrogenation. Consequently, the interfacial sites on a Pd/In_2O_3 catalyst would contribute more significantly to methanol formation.

3.3.2. RWGS route

Fig. 6 shows the potential energy surface of the RWGS route for methanol synthesis from CO_2 hydrogenation. The RWGS route initiates by the hydrogenation of adsorbed CO_2 to yield trans-COOH. This reaction is endothermic by +0.21 eV with an activation barrier

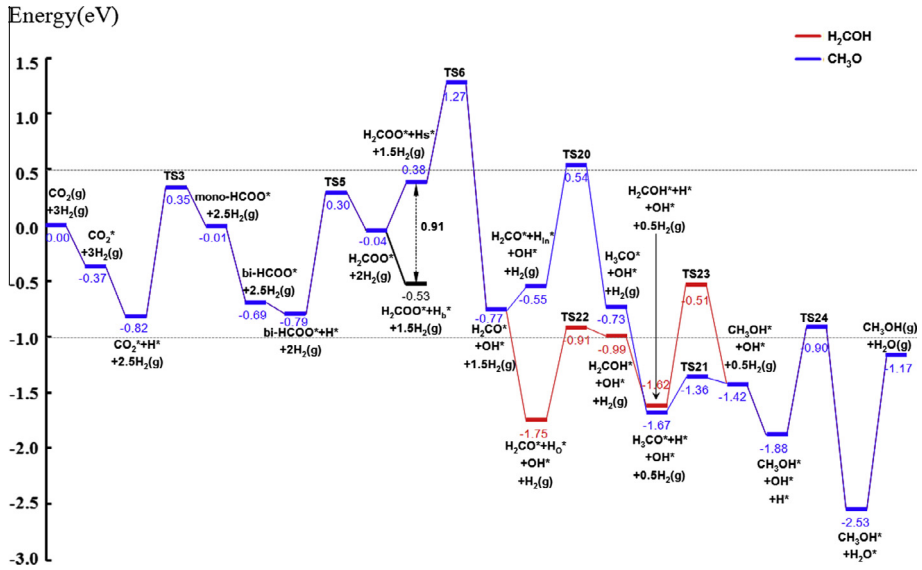

Fig. 5. Potential energy surface of CO_2 hydrogenation to methanol on Pd_4/In_2O_3 through formate route. Red line: H_2COH pathway, blue line: CH_3O pathway. (For interpretation of the references to color in this figure legend, the reader is referred to the web version of this article.)

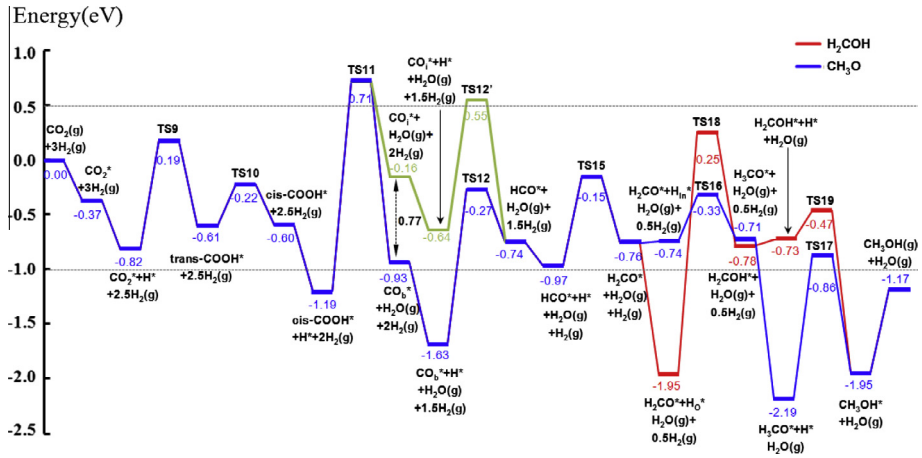

Fig. 6. Potential energy surface of CO_2 hydrogenation to methanol on Pd_4/In_2O_3 through RWGS route. Red line: H_2COH pathway, blue line: CH_3O pathway. (For interpretation of the references to color in this figure legend, the reader is referred to the web version of this article.)

of 1.01 eV. The trans-COOH is as stable as cis-COOH. As a result, the transformation between trans-COOH and cis-COOH is energetically neutral and only needs to climb an activation barrier of 0.39 eV. The cleavage of the C–O bond of CO_2 is the key step in RWGS route. There are two possible reactions that lead to the C–O bond breaking: one is the hydrogenation of COOH through R11 (cis-COOH* + H* → CO* + H_2O(g), ΔE = +0.26 eV, E_a = 1.90 eV) and another is the decomposition of COOH to CO and OH (E_a > 2.40 eV). Obviously, although both reactions are not feasible, the COOH hydrogenation is more favorable than COOH decomposition. CO produced from these reactions adsorbs on Pd_4/In_2O_3 in two forms CO_b^* and CO_i^*, and the structures are shown in support information (Fig. S1). CO_b^* represents a CO molecule adsorbs on the supported Pd_4 cluster at the Pd–Pd bridge site with an adsorption energy of −1.65 eV and CO_i^* represents a CO molecule that adsorbs at the interface of Pd_4/In_2O_3 catalyst with an adsorption energy of −0.88 eV. The hydrogenation of CO to produce HCO goes through either R12 (CO_b^* + H* → HCO* + *, ΔE = +0.89 eV, E_a = 1.36 eV) or R12′ (CO_i^* + H* → HCO* + *, ΔE = −0.10 eV, E_a = 1.19 eV) pathway. HCO produced from CO_i^* is both thermodynamically and kinetically more favorable than HCO produced from CO_b^*. However, the strong adsorption of CO_b^* indicates that the probability of finding CO_b^* is much higher than that of finding CO_i^*, and that transformation of CO_i^* to CO_b^* is energetically favorable. In addition, the potential energy profile of CO hydrogenation to HCO through CO_b^* is below that through CO_i^*. As a result, HCO prefers to be produced from hydrogenation of CO_b^* instead of CO_i^*. The following step is hydrogenation of HCO to H_2CO through R15 (HCO* + H* → H_2CO^* + *, ΔE = +0.21 eV, E_a = 0.82 eV). Further hydrogenation of H_2CO to produce CH_3OH also has two reaction pathways, similar to that in the formate route. The H_3CO pathway is through reactions R16 (H_2CO^* + H* → H_3CO^* + *, ΔE = +0.03 eV, E_a = 0.41 eV) and R17 (H_3CO^* + H* → CH_3OH^* + *, ΔE = +0.24 eV, E_a = 1.33 eV). The H_2COH pathway is via reactions R18 (H_2CO^* + H* → H_2COH^* + *, ΔE = +1.17 eV, E_a = 2.20 eV) and R19 (H_2COH^* + H* → CH_3OH^* + *, ΔE = −1.22 eV, E_a = 0.26 eV). The apparent high activation barrier of R18 effectively blocks the H_2COH pathway. Furthermore, the potential energy surface of the CH_3O pathway is always below the H_2COH pathway. Therefore, methanol will mainly be produced through the CH_3O pathway in the RWGS route. Since the OH* species is removed by H_2O formation in R11, the tetrahedral structure of Pd_4 cluster transforms into a butterfly shape which is maintained

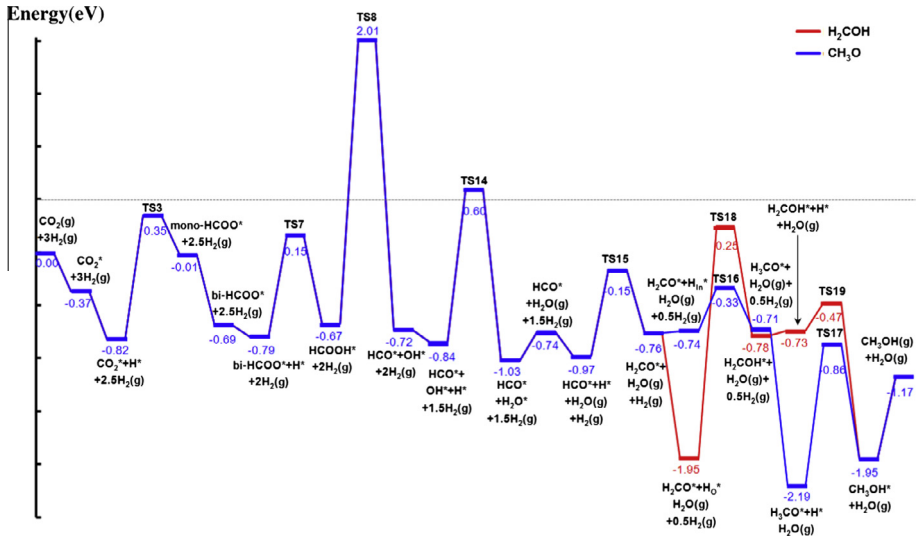

Fig. 7. Potential energy surface of CO_2 hydrogenation to methanol on Pd_4/In_2O_3 through formic acid route. Red line: H_2COH pathway, blue line: CH_3O pathway. (For interpretation of the references to color in this figure legend, the reader is referred to the web version of this article.)

in the subsequent reactions from H_2CO to produce CH_3OH. In the RWGS route, the rate-limiting step is the hydrogenation of COOH to produce CO and H_2O (R11).

3.3.3. HCOOH route

Fig. 7 shows the potential energy surface of the HCOOH route for methanol formation from CO_2 hydrogenation. In fact, this route connects both formate and RWGS routes. HCOOH can be formed from bi-HCOO hydrogenation but not from trans(cis)-COOH hydrogenation due to the steric hindrance (see Fig. S1). In the HCOOH route, CO_2 goes through the same hydrogenation step to bi-HCOO as it did in the formate route. Protonation of bi-HCOO leads to HCOOH formation. This reaction is slightly endothermic by 0.12 eV, with an activation barrier of 0.94 eV. HCOOH binds to the In_2O_3 surface through a single In–O bond with a binding energy of 0.52 eV. To produce methanol, HCOOH needs to dissociate to HCO^* and OH^*. The reaction energy of this step is almost zero, but the activation barrier is 2.68 eV. This activation barrier is significantly higher than the adsorption energy of HCOOH, which will likely results in desorption of the HCOOH species.

We note that many factors may contribute to the observed reactivity and selectivity of a working catalyst and a Pd_4/In_2O_3 model has its limitations in representing all the aspects of a practical Pd/In_2O_3 catalyst. In order to test the influence of the cluster size, we examined the rate-limiting steps in the HCOO and RWGS routes on a Pd_{13}/In_2O_3 model system. In this case, we focused on similar sites to those on Pd_4/In_2O_3 and determined the reaction energies and activation barriers of the corresponding elementary steps. The structural details and reaction energetics are shown in Fig. S3 and Table S2. The activation barriers of both R6′ ($H_2COO^* + H_b^* \rightarrow H_2CO^* + OH^*$, $\Delta E = -0.73$ eV, $E_a = 1.72$ eV) and R11′ (cis-$COOH^* + H^* \rightarrow CO^* + H_2O$ (g), $\Delta E = -0.41$ eV, $E_a = 1.79$ eV) are slightly lower than those on Pd_4/In_2O_3 (R6: $E_a = 1.80$ eV; R11: $E_a = 1.90$ eV, without taking the pre-activation of H adatoms into account). More importantly, R6′ and R11′ are still competitive for the interfacial reactions. These results indicate that the interfacial sites of Pd_{13}/In_2O_3 exhibit a similar activity to that of Pd_4/In_2O_3.

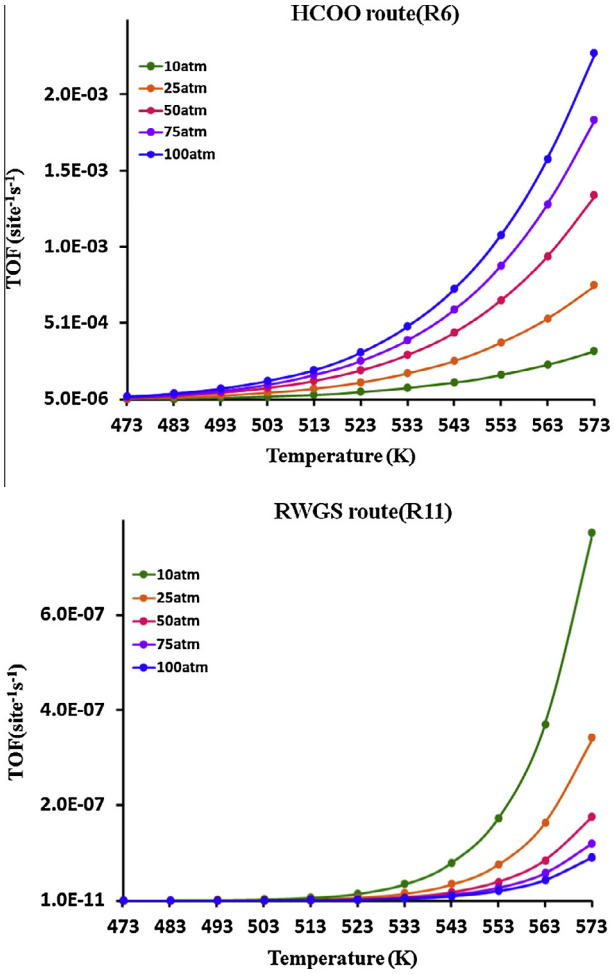

Fig. 8. Temperature dependence of TOF of R6 in HCOO route and R11 in RWGS route under varied pressure, respectively. The CO_2 conversion is $x = 0.0522$.

3.3.4. Microkinetic model

So far, we analyzed the methanol synthesis on Pd_4/In_2O_3 through the HCOO, RWGS and HCOOH routes based on the energetic data from the DFT calculations. The DFT results indicate that the HCOO and RWGS pathways can be considered as the competing reaction routes for methanol synthesis whereas the HCOOH

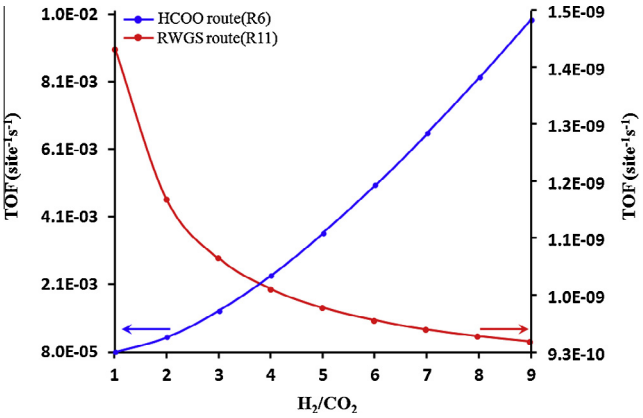

Fig. 9. H_2/CO_2 ratio dependence of TOF of R6 in HCOO route and R11 in RWGS route at 523 K, 50 atm. The CO_2 conversion is $x = 0.1075$.

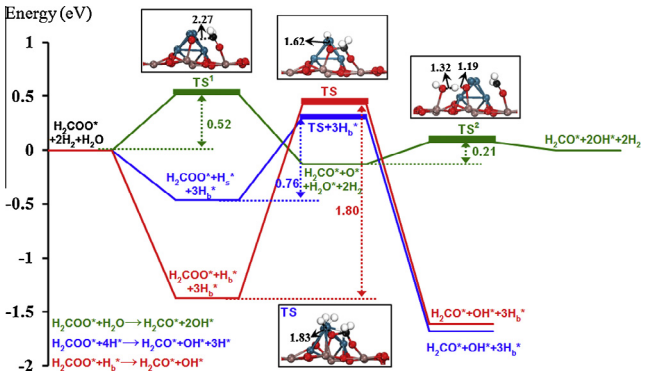

Fig. 10. Comparison of different ways for H_2COO hydrogenation to H_2CO.

route is unlikely to result in methanol. In this section, we will use a microkinetic model to analyze the dominant reaction mechanisms (HCOO and RWGS). The details of the analysis are provided in the supporting information. For comparison, a steady-state conversion of 0.0522 is chosen as the lowest equilibrium conversion of the overall reaction at a stoichiometric H_2/CO_2 ratio (3) in the temperature range of 473–573 K and pressure range of 10–100 atm. Fig. 8 shows the turn over frequency (TOF) of the rate-limiting step of R6 in the HCOO route and R11 in the RWGS route at different temperatures (473–573 K) and pressures (10–100 atm). For R6, the TOF varies from 5.0×10^{-6} to 2.0×10^{-3} site^{-1} s^{-1}, which is consistent with the measured [74] and calculated [75] TOF of methanol. The TOF of R6 increases with the increasing temperature under the same pressure and with the increasing pressure at the same temperature. For R11, the TOF varies from 1.0×10^{-11} to 8.0×10^{-11} site^{-1} s^{-1}. The TOF of R11 increases with the increasing temperatures under the same pressure but decreases with the increasing pressure at the same temperature. Comparing the HCOO route with the RWGS route, the rate of R6 is 4–5 orders of magnitude greater than that of R11, as shown in Fig. 8, which indicates that the methanol produced through HCOO route is significantly more than that from the RWGS route. This result also demonstrates that the dominant reaction mechanism in methanol synthesis is the HCOO route.

The effects of the H_2/CO_2 ratio on the reaction rate of R6 in the HCOO route and R11 in the RWGS route have also been analyzed. Fig. 9 shows the variation of TOF of R6 in HCOO route and R11 in RWGS route with the H_2/CO_2 ratio at 523 K, 50 atm, a CO_2 conversion of 0.1075. The TOF of R6 increases with the increasing H_2/CO_2 ratio. In contrast, the TOF of R11 decreases with the increasing H_2/CO_2 ratio. These results show that increasing the concentration of H_2 results in an increase of the reaction rate of R6 but a decrease of the reaction rate of R11, which suggests that the RWGS route could be suppressed by a high H_2/CO_2 ratio.

To summarize, the complete reaction pathways for methanol synthesis from CO_2 hydrogenation have been studied both thermodynamically and kinetically. From the thermodynamic perspective, the HCOO and RWGS routes are the most likely reaction mechanisms for methanol synthesis. The HCOOH route is suppressed due to a high activation barrier. In addition, the HCOO and RWGS routes are competitive. From a kinetic perspective, the reaction rate of the rate-limiting step in HCOO route is 4–5 orders of magnitude bigger than that of RWGS route, making the HCOO route the primary pathway for forming methanol. In addition, increasing the reaction temperature, pressure, and the H_2/CO_2 ratio can increase the reaction rate.

3.4. Effects of H coverage and H_2O

Hydrogenation of H_2COO to H_2CO through the reaction $H_2COO^* + H_b^* \rightarrow H_2CO^* + OH^*$ has an activation barrier of 1.80 eV. A large portion of the barrier originates from the activation of H_b^* to H_s^* from the most stable adsorption configurations. This model assumes that H atoms are added onto the Pd_4 cluster one by one for each hydrogenation step, corresponding to the condition of low H coverage throughout the reaction. Under such a condition, H atom prefers to adsorb at the bridge site instead of terminal site. As a result, activation of H from bridge site to terminal site is a necessary step for hydrogenating CO_2. In order to better understand the coverage effect of hydrogen, we introduced four H adatoms onto the Pd_4 cluster at the same time to simulate a high H coverage situation. Since four H adatoms is the minimum coverage which could make the H adatom stably adsorb at the terminal site. In this case, three H adatoms bind the Pd_4 cluster at bridge sites (H_b^*) and one at the terminal site (H_s^*). Under such a high H coverage, one of the H adatoms is already in the activated state, effectively lowering the barrier for the hydrogenation step to 0.76 eV, as shown by the blue line in Fig. 10. Therefore, increasing the hydrogen partial pressure will increase the H_s^* coverage and promote methanol production via the formate route. As the hydrogen coverage is increased, the H^* adatoms will be forced to the terminal sites, making them available for hydrogenating the adsorbed CO_2 and intermediates. We note that the energy of the $H_2COO^* + H_b^* + 3H_b^*$ (red[1]) state is lower than $H_2COO^* + H_s^* + 3H_b^*$ (blue) state in Fig. 10. The energy difference corresponds to the upper bound of the energy needed to activate H adatom on Pd_4 at a low coverage (one H adatom on the cluster) since the $H_2COO^* + H_b^* + 3H_b^*$ (red) state was calculated by treating all 4 H_b^* having the same adsorption energy. The state with all 4 hydrogen adatoms occupying the bridge sites on Pd_4 unlikely exists since H adatoms may be moved from bridge to terminal site at high H adatom coverages. On the other hand, this treatment maintains the mass balance while allows a comparison with the energy of the $H_2COO^* + H_s^* + 3H_b^*$ (blue) state.

The presence of water in methanol synthesis from CO_2 hydrogenation cannot be avoided since it is the one of the products. The effect of water on methanol synthesis depends strongly on the catalyst and substrates. In this work, H_2O was shown to promote production of H_2CO from H_2COO, which initially went through the $H_2COO^* + {}^* \rightarrow H_2CO^* + O^*$ reaction ($E_a = 0.52$ eV), followed by the $H_2CO^* + O^* + H_2O^* \rightarrow H_2CO^* + 2OH^*$ reaction ($E_a = 0.21$ eV). As a result, the overall reaction barrier is 0.73 eV with H_2O promotion, as shown by the green line in Fig. 10. Furthermore, the presence of water will also promote methanol production kinetically. As water

[1] For interpretation of color in Fig. 10, the reader is referred to the web version of this article.

is produced as the reaction progresses, it will have an autocatalytic effect of methanol formation. However, since water is on the product side of the reaction, excessive amount of water will drive the balance to the reactant side. Consequently, the amount of water in a reactor has to be optimized to achieve best performance toward the methanol production. In fact, the existence of H_2O does not only promote the hydrogenation of H_2COO but also prevents the hydrogenation of COOH to CO and water [20]. Experimental observation suggested that H_2O promotes the hydrogenation of HCOO to methanol [76]. Theoretical studies reported that H_2O facilitates the formation of trans-COOH, which was considered as a bottleneck step in the hydrocarboxyl mechanism [45].

3.5. Effect of OH on the structure of supported Pd_4

In the formate route, OH adsorbs at the interface of Pd/In_2O_3 until the last step. It is then combines with H to form H_2O and desorbs. In the entire process, the Pd_4 cluster maintains a tetrahedral structure. On the other hand, the adsorbed OH combines with the H adatom to form H_2O and desorbs once OH is generated in the RWGS route. In this case, the Pd_4 cluster maintains a butterfly shape. These results show that the presence of adsorbed OH at the interface helps to maintain the Pd_4 cluster in the tetrahedron form, whereas the desorption of OH in the form of H_2O caused a structural transformation of the Pd_4 cluster to a butterfly shape. When the Pd_4 cluster is in the tetrahedral shape, the H_2COH pathway is more favorable than H_3CO, as shown in Fig. 5. However, once the Pd_4 cluster is transformed into a butterfly shape, the H_3CO reaction pathway becomes more favorable than H_2COH, as shown in Fig. 6. As a result, the Pd_4 cluster with different structures exhibits different activities for producing CH_3OH from H_2CO. The structural flexibility and responsiveness of the supported metal nanoparticles under reactive environment can ultimately determine the nature and efficacy of the chemical and catalytic processes, as documented in the recent reviews [33,34,77].

4. Conclusions

In the present work, we combined DFT calculations and microkinetic modeling to study the reaction mechanism of methanol synthesis from CO_2 hydrogenation on a Pd_4/In_2O_3 model catalyst. Our results show that the interface is the most active site for CO_2 adsorption and hydrogenation. Furthermore, a high barrier for CO_2 dissociation on Pd_4/In_2O_3 excludes CO as a key intermediate species for methanol synthesis and prevents the poison of the interfacial sites by O adatoms. Among three possible reaction routes, the HCOO and RWGS routes are competitive pathways for methanol formation from CO_2 hydrogenation, whereas the HCOOH route is highly unlikely due to the high activation barrier, according to our DFT results. Microkinetic modeling of the rate-limiting steps in HCOO and RWGS routes further identifies that the HCOO route is the dominant pathway.

Key operating parameters influencing the reaction have been proposed through the combined DFT and microkinetic study. The DFT results showed that the presence of activated H adatoms, therefore, high hydrogen partial pressure, and coadsorbed H_2O benefit methanol synthesis by lowering the activation barriers of the rate-limiting step in the HCOO route. Kinetic modeling indicated that increasing the reaction temperature, pressure and the H_2/CO_2 ratio increases the overall reaction rate. The study also demonstrated the dynamical nature of the structure of the supported catalyst. The structure of the supported Pd_4 cluster transforms in response to the presence of OH in the reaction environment, which is accompanied by a switch of the reaction pathway from favoring the H_2COH pathway in HCOO route to the CH_3O pathway in RWGS route.

In summary, the combined DFT and kinetic study demonstrated the importance of the metal/support interface to CO_2 hydrogenation as well as the dynamical nature of the supported metal catalyst during a reaction. The reactivity and selectivity can be optimized by effectively control the size and morphology of the metal particles on the substrates. Furthermore, the knowledge on the operating variables such temperature, pressure and composition of the feed gas will be a useful guide to the experimental study.

Acknowledgments

We gratefully acknowledge the supports from the National Natural Science Foundation of China (#91334206) and from U.S. Department of Energy, Basic Energy Science program (DE-FG02-05ER46231). D. Mei was supported by the U.S. Department of Energy, Office of Basic Energy Sciences, Division of Chemical Sciences, Geosciences & Biosciences. The computations were performed in part using the Molecular Science Computing Facility in the William R. Wiley Environmental Molecular Sciences Laboratory (EMSL), which is a U.S. Department of Energy national scientific user facility located at PNNL in Richland, Washington.

Appendix A. Supplementary material

Supplementary data associated with this article can be found, in the online version, at http://dx.doi.org/10.1016/j.jcat.2014.06.002.

References

[1] G.A. Olah, G.K.S. Prakash, A. Goeppert, J. Am. Chem. Soc. 133 (2011) 12881.
[2] H. Arakawa, M. Aresta, J.N. Armor, M.A. Barteau, E.J. Beckman, A.T. Bell, J.E. Bercaw, C. Creutz, E. Dinjus, D.A. Dixon, K. Domen, D.L. DuBois, J. Eckert, E. Fujita, D.H. Gibson, W.A. Goddard, D.W. Goodman, J. Keller, G.J. Kubas, H.H. Kung, J.E. Lyons, L.E. Manzer, T.J. Marks, K. Morokuma, K.M. Nicholas, R. Periana, L. Que, J. Rostrup-Nielson, W.M.H. Sachtler, L.D. Schmidt, A. Sen, G.A. Somorjai, P.C. Stair, B.R. Stults, W. Tumas, Chem. Rev. 101 (2001) 953.
[3] Y. Yang, C.A. Mims, D.H. Mei, C.H.F. Peden, C.T. Campbell, J. Catal. 298 (2013) 10.
[4] Q. Ge, Mechanistic understanding of catalytic CO_2 activation from first principles theory, in: S.L. Suib (Ed.), New and Future Developments in Catalysis, Elsevier, Amsterdam, 2013.
[5] T. Fujitani, M. Saito, Y. Kanai, T. Watanabe, J. Nakamura, T. Uchijima, Appl. Catal. A 125 (1995) L199.
[6] S. Imamura, K. Denpo, K. Utani, Y. Matsumura, H. Kanai, React. Kinet. Catal. Lett. 67 (1999) 163.
[7] X.-L. Liang, X. Dong, G.-D. Lin, H.-B. Zhang, Appl. Catal. B 88 (2009) 315.
[8] T. Fujitani, I. Nakamura, Bull. Chem. Soc. Jpn. 75 (2002) 1393.
[9] A.L. Bonivardi, D.L. Chiavassa, C.A. Querini, M.A. Baltanása, Stud. Surf. Sci. Catal. 130 (2000) 3747.
[10] N. Iwasa, T. Mayanagi, N. Ogawa, K. Sakata, N. Takezawa, Catal. Lett. 54 (1998) 119.
[11] N. Iwasa, T. Mayanagi, W. Nomura, M. Arai, N. Takezawa, Appl. Catal. A 248 (2003) 153.
[12] G. Frank, H. Köstlin, Appl. Phys. A 27 (1982) 197.
[13] S. Lany, A. Zunger, Phys. Rev. Lett. 98 (2007) 045501.
[14] P. Agoston, K. Albe, Phys. Chem. Chem. Phys. 11 (2009) 3226.
[15] I. Djerdj, A. Haensch, D. Koziej, S. Pokhrel, N. Barsan, U. Weimar, M. Niederberger, Chem. Mater. 21 (2009) 5375.
[16] I. Tanaka, F. Oba, K. Tatsumi, M. Kunisu, M. Nakano, H. Adachi, Mater. Trans. 43 (2002) 1426.
[17] T. Umegaki, K. Kuratani, Y. Yamada, A. Ueda, N. Kuriyama, T. Kobayashi, Q. Xu, J. Power Sources 179 (2008) 566.
[18] T. Bielz, H. Lorenz, P. Amann, B. Klotzer, S. Penner, J. Phys. Chem. C 115 (2011) 6622.
[19] J. Ye, C. Liu, D. Mei, Q. Ge, ACS Catal. 3 (2013) 1296.
[20] J. Ye, C. Liu, Q. Ge, J. Phys. Chem. C 116 (2012) 7817.
[21] T. Bielz, H. Lorenz, W. Jochum, R. Kaindl, F. Klauser, B. Klötzer, S. Penner, J. Phys. Chem. C 114 (2010) 9022.
[22] H. Lorenz, W. Jochum, B. Klötzer, M. Stöger-Pollach, S. Schwarz, K. Pfaller, S. Penner, Appl. Catal. A 347 (2008) 34.
[23] Y. Men, G. Kolb, R. Zapf, M. O'Connell, A. Ziogas, Appl. Catal. A 380 (2010) 15.
[24] N. Iwasa, N. Takezawa, Top. Catal. 22 (2003) 215.
[25] H. Lorenz, S. Turner, O.I. Lebedev, G. Van Tendeloo, B. Klötzer, C. Rameshan, K. Pfaller, S. Penner, Appl. Catal. A 374 (2010) 180.
[26] F.A. Marchesini, S. Irusta, C. Querini, E. Miró, Appl. Catal. A 348 (2008) 60.

[27] J. Ye, C. Liu, Q. Ge, Phys. Chem. Chem. Phys. 14 (2012) 16660.
[28] N. Iwasa, H. Suzuki, M. Terashita, M. Arai, N. Takezawa, Catal. Lett. 96 (2004) 75.
[29] S.E. Collins, M.A. Baltanás, A.L. Bonivardi, J. Phys. Chem. B 110 (2006) 5498.
[30] S. Collins, J.J. Delgado, C. Mira, J.J. Calvino, S. Bernal, D.L. Chiavassa, M.A. Baltanása, A.L. Bonivardi, J. Catal. 292 (2012) 90.
[31] S. Collins, D. Chiavassa, A. Bonivardi, M. Baltanás, Catal. Lett. 103 (2005) 83.
[32] J.H. Kwak, L. Kovarik, J. Szanyi, ACS Catal. 3 (2013) 2094.
[33] M. Flytzani-Stephanopoulos, B.C. Gates, Annu. Rev. Chem. Biomol. Eng. 3 (2012) 545.
[34] A. Kulkarni, R.J. Lobo-Lapidus, B.C. Gates, Chem. Commun. 46 (2010) 5997.
[35] X.-F. Yang, A. Wang, B. Qiao, J. Li, J. Liu, T. Zhang, Acc. Chem. Res. 46 (2013) 1740.
[36] G. Kwon, G.A. Ferguson, C.J. Heard, E.C. Tyo, C. Yin, J. DeBartolo, S. Seifert, R.E. Winans, A.J. Kropf, J. Greeley, R.L. Johnston, L.A. Curtiss, M.J. Pellin, S. Vajda, ACS Nano 7 (2013) 5808.
[37] B. Qiao, A. Wang, X. Yang, L.F. Allard, Z. Jiang, Y. Cui, J. Liu, T. Zhang, Nat. Chem. 3 (2011) 634.
[38] S.E. Collins, M.A. Baltanás, J.L. Garcia Fierro, A.L. Bonivardi, J. Catal. 211 (2002) 252.
[39] R.C. Baetzold, Surf. Sci. 51 (1975) 1.
[40] J. Moc, D.G. Musaev, K. Morokuma, J. Phys. Chem. A 104 (2000) 11606.
[41] V.A. Matsura, N.S. Panina, V.V. Potekhin, V.B. Ukraintsev, K.A. Khokhryakov, V.V. Platonov, O.M. Tatsenko, A.I. Panin, Russ. J. Gen. Chem. 74 (2004) 975.
[42] Y.-X. Pan, C.-J. Liu, Q. Ge, J. Catal. 272 (2010) 227.
[43] L.C. Grabow, M. Mavrikakis, ACS Catal. 1 (2011) 365.
[44] Y. Yang, J. Evans, J.A. Rodriguez, M.G. White, P. Liu, Phys. Chem. Chem. Phys. 12 (2010) 9909.
[45] Y.-F. Zhao, Y. Yang, C. Mims, C.H.F. Peden, J. Li, D. Mei, J. Catal. 281 (2011) 199.
[46] Y. Yang, M.G. White, P. Liu, J. Phys. Chem. C 116 (2011) 248.
[47] Y.-F. Zhao, R. Rousseau, J. Li, D. Mei, J. Phys. Chem. C 116 (2012) 15952.
[48] M. Cargnello, V.V.T. Doan-Nguyen, T.R. Gordon, R.E. Diaz, E.A. Stach, R.J. Gorte, P. Fornasiero, C.B. Murray, Science 341 (2013) 771.
[49] S. Abbet, A. Sanchez, U. Heiz, W.D. Schneider, A.M. Ferrari, G. Pacchioni, N. Rösch, J. Am. Chem. Soc. 122 (2000) 3453.
[50] S. Sirois, M. Castro, D.R. Salahub, Int. J. Quantum Chem. 52 (1994) 645.
[51] M.-P. Habas, F. Mele, M. Sodupe, F. Illas, Surf. Sci. 431 (1999) 208.
[52] J.M. Seminario, A.G. Zacarias, M. Castro, Int. J. Quantum Chem. 61 (1997) 515523.
[53] G. Kresse, J. Hafner, Phys. Rev. B 48 (1993) 13115.
[54] G. Kresse, J. Furthmüller, Phys. Rev. B 54 (1996) 11169.
[55] G. Kresse, D. Joubert, Phys. Rev. B 59 (1999) 1758.
[56] J.P. Perdew, K. Burke, M. Ernzerhof, Phys. Rev. Lett. 77 (1996) 3865.
[57] P.E. Blochl, Phys. Rev. B 50 (1994) 17953.
[58] G. Henkelman, H. Jónsson, J. Chem. Phys. 113 (2000) 9978.
[59] X. Dong, H.-B. Zhang, G.-D. Lin, Y.-Z. Yuan, K.R. Tsai, Catal. Lett. 85 (2003) 237.
[60] M.C. Valero, P. Raybaud, P. Sautet, J. Catal. 247 (2007) 339.
[61] M.C. Valero, P. Raybaud, P. Sautet, Phys. Rev. B 75 (2007) 045427.
[62] E. Kaxiras, Atomic and Electronic Structure of Solids, Cambridge University Press, Cambridge, 2003. p. 198.
[63] C. Kittel, Introduction to Solid State Physics, eighth ed., John Wiley & Sons Inc., Hoboken, NJ, 2005. p. 50.
[64] C.T. Campbell, S.C. Parker, D.E. Starr, Science 298 (2002) 811.
[65] S.E. Wanke, P.C. Flynn, Catal. Rev. 12 (1975) 93.
[66] R. Ouyang, J.-X. Liu, W.-X. Li, J. Am. Chem. Soc. 135 (2013) 1760.
[67] J.M. Rickard, L. Genovese, A. Moata, S. Nitsche, J. Catal. 121 (1990) 141.
[68] A.T. Bell, Science 299 (2003) 1688.
[69] Y. Li, G.A. Somorjai, Nano Lett. 10 (2010) 2289.
[70] Q.L. Tang, Q.J. Hong, Z.P. Liu, J. Catal. 263 (2009) 114.
[71] A. Sotiropoulos, P.K. Milligan, B.C.C. Cowie, M. Kadodwala, Surf. Sci. 444 (2000) 52.
[72] G. Peng, S.J. Sibener, G.C. Schatz, S.T. Ceyer, M. Mavrikakis, J. Phys. Chem. C 116 (2012) 3001.
[73] T. Fujitani, Y. Choi, M. Sano, Y. Kushida, J. Nakamura, J. Phys. Chem. B 104 (2000) 1235.
[74] G.H. Graaf, E.J. Stamhuis, A.A.C.M. Beenackers, Chem. Eng. Sci. 43 (1988) 3185.
[75] T.S. Askgaard, J.K. Norskov, C.V. Ovesen, P. Stoltze, J. Catal. 156 (1995) 229.
[76] Y. Yang, C.A. Mims, R.S. Disselkamp, J.-H. Kwak, C.H.F. Peden, C.T. Campbell, J. Phys. Chem. C 114 (2010) 17205.
[77] M.A. Newton, Chem. Soc. Rev. 37 (2008) 2644.